Comparison of measured brightness temperatures from SMOS with modelled ones from ORCHIDEE and H-TESSEL over the Iberian Peninsula

A. Barella-Ortiz[1,5], J. Polcher[1,5], P. de Rosnay[2], M. Piles[3] and E. Gelati[4,5]

[1]{Laboratoire de Météorologie Dynamique du CNRS, IPSL, École Polytechnique, Université Paris-Saclay, France}

[2]{European Centre for Medium-Range Weather Forecasts, Reading, UK}

[3]{Dept. de Teor. del Senyal i Comunicacions, Univ. Politec. de Catalunya, Barcelona, Spain}

[4]{CNRM-GAME (Météo-France, CNRS), Toulouse, France}

[5]{Centre National de la Recherche Scientifique (CNRS)}

Correspondence to: A. Barella-Ortiz (Anais.Barella-ortiz@lmd.jussieu.fr)

Abstract

L-Band radiometry is considered to be one of the most suitable techniques to estimate Surface Soil Moisture (SSM) by means of remote sensing. Brightness temperatures are key in this process, as they are the main input in the retrieval algorithm which yields SSM estimates. The work exposed compares brightness temperatures measured by the SMOS mission to two different sets of modelled ones, over the Iberian Peninsula from 2010 to 2012. The two modelled sets were estimated using a radiative transfer model and state variables from two land surface models: i) ORCHIDEE and ii) H-TESSEL. The radiative transfer model used is the CMEM.

Measured and modelled brightness temperatures show a good agreement in their temporal evolution, but their spatial structures are not consistent. An Empirical Orthogonal Function analysis of the brightness temperature's error identifies a dominant structure over the southwest of the Iberian Peninsula which evolves during the year and is maximum in fall and winter. Hypotheses concerning forcing induced biases and assumptions made in the radiative

transfer model are analyzed to explain this inconsistency, but no candidate is found to be responsible for the weak spatial correlations at the moment. Further hypotheses are proposed and will be explored in a forthcoming paper. The analysis of spatial inconsistencies between modelled and measured TBs is important, as these can affect the estimation of geophysical variables, TB assimilation in operational models, as well as result in misleading validation studies.

1 Introduction

The United Nations (UN), the Food and Agriculture Organization (FAO), and the World Health Organization (WHO), have reported that water resources are not being managed in an optimum way at present. As a result, scarcity, hygiene and pollution issues related to improper water policies are detected. In addition, the world's population is expected to grow by 2 to 3 billion people over the next 40 years according to the UN's World Water Development Report from 2012 (WWAP, 2012). This will lead to a significant increase in freshwater demand which will likely be affected by the effect of a changing climate.

To achieve a better management of water resources, it is necessary to improve our understanding of hydrological processes. In order to do this, the study of Soil Moisture (SM) is essential. It is defined as the water content in the soil and has a key role on the soil-atmosphere interface. SM determines whether evaporation over land surfaces occurs at a potential rate (controlled by atmospheric conditions) or if it is limited by the available moisture (Milly, 1992). In addition, it influences several processes, like infiltration and surface temperature, which have an important effect on plant growth and the general state of the continental surfaces. However, SM is a complex variable to model as the interactions between soils and water are not simple to represent. Its definition requires knowledge of soil hydraulic conductivity, which are not often available as direct measurements. These are used to access the saturated and residual soil water content, as well as for SM dynamics. Pedo-transfer functions (Marthews et al., 2014), allow to estimate hydrodynamic characteristics of the soil from available soil texture and structure information. However, the suitability of these functions is under debate (Baroni et al., 2008), as their performance depends on several factors like the climate, geology, and the measurement techniques used. Furthermore, different hydrological schemes are found in Land Surface Models (LSM), leading to various ways of understanding and formulating soil moisture.

Remotely sensed soil moisture products have brought about new ways to perform data retrieval, adding new observations to data assimilation chains. The optimal combination of these products with modelled ones is expected to provide better estimates of the true soil moisture state. Remote sensing allows to estimate SM by means of retrieval algorithms, like inversion algorithms (Kerr et al., 2012) or neural networks (Kolassa et al., 2013). Their main input depends on the type of sensor used. This is, backscattering for an active sensor and Brightness Temperature (TB) for a passive sensor. TB corresponds to the radiance emitted by the Earth at a given wavelength and is the magnitude measured by a radiometer. It is defined as the physical temperature times the emissivity of the surface.

L-Band radiometry is one of the best methods to estimate soil moisture, due to the relation between SM and the soil dielectric constant (ϵ) in this wavelength. The latter differs significantly between a dry soil and water (4 vs. 80, respectively) and this difference is key to estimate the soil water content. It should be noted that the retrieved SM corresponds to the water contained in the first centimetres of the soil. The penetration depth in averaged conditions is about 5 cm (Kerr et al., 2010). Therefore, we will refer to Surface Soil Moisture (SSM) instead of soil moisture. Some studies, like Escorihuela et al. (2010) lower the penetration depth to 1–2 cm.

In the last decade, three space missions have been launched with L-Band radiometers on-board: the Soil Moisture and Ocean Salinity (SMOS) mission (Kerr et al., 2010), the Aquarius/SAC-D mission (Le Vine et al., 2010), and the Soil Moisture Active and Passive (SMAP) mission (Entekhabi et al., 2010).

A large number of validation studies of remotely sensed SSM products have been carried out (Albergel et al., 2011; Sánchez et al., 2012; Bircher et al., 2013). These studies are usually performed using airborne and or ground-observed data over a well equipped site. Other studies, like the one described in González-Zamora et al. (2015), validate SMOS SSM products using in situ soil moisture measurement networks, which allow to extend the study period to annual and inter-annual scales. Several studies have been performed to validate brightness temperatures too (Rüdiger et al., 2011; Montzka et al. 2013). In Bircher et al. (2013) TBs are also validated with network and airborne data over a SMOS pixel in the Skjern river Catchment (Denmark). LSMs coupled to Radiative Transfer Models (RTMs) can contribute to the analysis and validation of passive Microwave (MW) data. Models permit extending the validation to a longer period of time and perform an extensive analysis of observed and retrieved data, as shown in Schlenz et al. (2012). In this study, they compare TBs and vegetation optical depth from SMOS with modelled ones obtained from a LSM coupled to a radiative transfer model, over a period of seven months in 2011 in the Vils test site (Germany). Comparing modelled with satellite-measured brightness temperatures can help to better understand inconsistencies between retrieved and modelled data. It provides information regarding the origin of their differences, and whether they are due to the retrieval algorithm or to issues related to the modelling process.

Polcher et al. (2016) present the first comparison of the spatial patterns of Level 2 (L2) SMOS product corresponding to retrieved SSM, with SSM modelled by the ORganising Carbon and Hydrology In Dynamic EcosystEms (ORCHIDEE) LSM (de Rosnay and Polcher, 1998; Krinner et al., 2005) over the Iberian Peninsula (IP) from 2010 to 2012. They identify inconsistencies between the spatial structures of retrieved and modelled SSM. The main objective of the work presented herein is to extend the analysis of this inconsistency by comparing brightness temperatures measured by SMOS (Level 1C, L1C, product) with modelled ones obtained from the coupling of ORCHIDEE's state variables and a RTM. In addition, a second set of modelled TBs using state variables from the Hydrology – Tiled ECMWF Scheme for Surface Exchanges over Land (H-TESSEL), is included in the comparison. The RTM used is the Community Microwave Emission Model (CMEM) [de Rosnay et al., 2009], developed by the European Centre for Medium-Range Weather Forecasts (ECMWF). The comparison is performed over the same period and region as the study carried out by Polcher et al. (2016). The IP is an excellent test case for remote sensing of SSM, as its two characteristic climate regimes (oceanic and Mediterranean) result in a strong contrast in soil water content. Furthermore, SSM is a critical variable regarding water resources especially in the IP, which makes this study even more necessary.

The data from SMOS and the LSMs used in this paper will be presented in the next section. A methodology section follows describing the data filtering and sampling processes carried out, together with the analysis performed to compare TBs. Afterwards, results will be presented. First, modelled and measured TBs will be compared. Second, their difference will be characterised spatially and temporally and certain hypotheses to explain the differences found in the TB comparison will be analyzed. Third, we will study the amplitude of the annual cycle of the TB signals. The paper will end with discussion and conclusion sections.

2 Data

2.1 SMOS retrievals of TB

The SMOS mission is the second Earth Explorer Opportunity mission from the European Spatial Agency (ESA). The SMOS satellite was launched on November 2nd, 2009. One of its main objectives is to provide surface soil moisture over land with a target accuracy of 0.04 m^3m^{-3}.

TBs are the main input of SMOS’s soil moisture retrieval algorithm. L-band brightness temperatures are measured by the SMOS radiometer at different incidence angles (from 0 to 65º) and polarizations (H, V, HV). The retrieval algorithm also models TBs using the state-of-the-art L-band Microwave Emission of the Biosphere (L-MEB) forward model (Wigneron et al., 2007) with some modifications. These brightness temperatures are then used to retrieve SSM using an inversion algorithm based on an iterative approach. Its objective is to minimize the sum of the squared weighted differences between measured and modelled TBs for all available incidence angles. Details about the retrieval algorithm are provided in Kerr et al. (2012).

The L1C product containing horizontally and vertically polarized brightness temperatures, was provided by the SMOS Barcelona Expert Center. From now on, this product will be referred to as TB_{SM}.

The SMOS L1C v5.05 product over the 10W : 5W to 45N : 35N region was selected and SMOS TBs at the antenna reference plane were derived: TBs were first screened out for Radio-Frequency Interferences (RFIs) (strong, point source and tails), and also for Sun (glint area, aliases and tails), and Moon (aliases) contamination, using the corresponding flags. Ionospheric effects (geometric and Faraday rotations) were later corrected to obtain TB at the Top Of the Atmosphere (TOA). TB maps at a constant incidence angle of 42.5±5° were obtained through chi squared linear fit of all values included in the interval 42.5±5°, which is the methodology used to generate the SMOS L1C browse product (McMullan et al., 2008). Finally, these maps were resampled from the Icosahedral Snyder Equal Area (ISEA) 4H9 grid to a 0.25° regular latitude-longitude grid, to facilitate its manipulation.

2.2 Modelled TB: CMEM

The Community Microwave Emission Modelling (CMEM) Platform (de Rosnay et al., 2009), developed at ECMWF, is a forward operator for low frequency passive MW brightness temperatures of the surface. Its physics is based on that of the L-MEB forward model and the Land Surface Microwave Emission Model (LSMEM) [Drusch et al., 2001]. CMEM is characterized by its modular structure, which allows the user to choose among different physical configurations to compute TB's key parameters. Polarized brightness temperatures provided at TOA result from the contribution of three dielectric layers: atmosphere, soil and vegetation. Snow, also considered, is characterized as a single additional homogeneous layer.

The two sets of modelled TBs used in this study were estimated by means of the CMEM provided with state variables from i) ORCHIDEE, and ii) H-TESSEL simulations. From now on we will refer to these sets as TB_{OR} and TB_{HT}, respectively. TB_{OR} was computed specifically for this study, while TB_{HT} was provided by the ECMWF to widen the comparison between measured and modelled data. The CMEM configuration used to compute each set of TB is listed in Table 1. The table is divided into three configuration categories: physical, observing, and soil and atmospheric levels. Even though both sets have similar configurations, there are some differences which are explained below.

First, the “Physical configuration” of TB_{OR} was selected to be as similar as possible to TB_{HT}. However, they differ in the parameterization used to compute the smooth surface emissivity (ε_s). For TB_{HT} the reflectivity of the flat soil surface was computed following the Fresnel law (Ulaby et al., 1986), so it is expressed as a function of the soil dielectric constant and the observation incidence angle. This formulation considers the emission at the soil interface. As it is simple and affordable in computing time it is commonly used for microwave emission modelling and soil moisture retrieval, as well as for operational applications (e.g. Wigneron et al., 2007, de Rosnay et al., 2009). It assumes an a priori soil moisture sampling depth, which in this study corresponds to the first soil layer of the land surface model (7cm for H-TESSEL). For TB_{OR}, the multilayered soil hydrology of ORCHIDEE allows to take into account the soil moisture profile and the resulting volume scattering effects on the soil emission. Therefore the reflectivity of the flat soil surface was computed using the parameterization proposed by Wilheit (1978). The different parameterizations chosen to calculate ε_s lead to another variation between the CMEM configurations. If ε_s is computed using Wilheit (1978), the soil temperature profile is used to compute the Effective

Temperature (T_{eff}). On the contrary, if the Fresnel law is used, the user can choose among different parameterizations to compute T_{eff}. For TB_{HT}, Wigneron et al. (2001) was selected.

Second, the “Observing configuration” considers different incidence angles for each set. Although the available TB_{HT} were modelled considering an angle of 40°, 42.5° was used to model TB_{OR}, because measured TBs were provided at this angle.

Third, a different number of soil layers was defined for the “Soil and atmospheric level configuration”: 11 (TB_{OR}) and 3 (TB_{HT}). ORCHIDEE's soil discretization is finer. For instance, its first layer's depth is of the order of millimetres, while H-TESSEL's is of centimetres. In order to evaluate the role of these differences in the vertical discretization and the LSMs, we performed a sensitivity analysis as detailed in the next paragraph.

In addition to the CMEM simulations performed to model TB_{OR} and TB_{HT} using the configurations indicated in Table 1, the following simulations were carried out to test if parameterization assumptions could affect the resulting TBs:

- Simulation 1: $TB_{HT(VC)}$, where the subscript “VC” stands for “Vegetation Cover”.

  Vegetation cover is a key input. Since this parameter is directly related to land-surface emissivity, the effects of a different vegetation cover were tested on TB_{HT}. For this matter, a new set of TBs was modelled using H-TESSEL's state variables with the same configuration as detailed in Table 1, except for the vegetation cover input, where H-TESSEL's prescribed vegetation (Boussetta et al., 2013) was considered. One of the differences between this input and the ECOCLIMAP database (used in the original configuration), is that the former consists of 20 vegetation types, while the latter considers 7.

- Simulation 2: $TB_{OR(SD)}$, where the subscript “SD” stands for “Soil Discretization”,

  The impact of a coarser soil representation on modelled TBs was tested by recomputing TB_{OR} using ORCHIDEE's state variables averaged to 3 soil layers: upper (9 cm), medium (66 cm), and lower (125 cm).

- Simulation 3: $TB_{OR(FW)}$, where the subscript “FW” stands for “Fresnel Wigneron”.

  We tested the combined effect of using the Fresnel law to compute ε_s, rather than the parameterization proposed by Wilheit (1978), and calculating T_{eff} using the methodology proposed by Wigneron (2001) instead of the soil temperature profile. For this, TBs were simulated using ORCHIDEE's state variables.

The input variables required by the CMEM to model TBs are summarized in Table 2. They are classified into dynamic and constant fields and consist of meteorological data, vegetation characteristics and soil conditions.

2.2.1 The ORCHIDEE and H-TESSEL Land Surface Models

ORCHIDEE

The ORCHIDEE LSM (de Rosnay and Polcher, 1998; Krinner et al., 2005) was developed by the Institut Pierre – Simon Laplace (IPSL). It can be run coupled with the general circulation model LMDZ, which was developed by the Laboratoire de Météorologie Dynamique (LMD), or in stand-alone mode. Uncoupled simulations were carried out for this study.

The hydrological scheme used by ORCHIDEE approaches hydrology through the resolution of a diffusive equation with a multilayer scheme. For this, the Fokker-Planck equation is solved over a soil 2 m deep with an 11 layer discretization. The layers' depths are informed in Table 1. The lower boundary condition is free drainage, under the hypothesis that the water content gradient between the last modelled layer and the next one (not modelled) is zero. The upper boundary condition sets the bare soil evaporation as the maximum upward hydrological flux which is permitted by diffusion if it is lower than potential evaporation.

The multilayer scheme considers a sub-grid variability of soil moisture, which together with the fine soil discretization improves the representation of infiltration processes. The soil infiltration follows the Green-Ampt equation (Green and Ampt, 1911) to represent the evolution in time of the wetting front through the soil layers. It should be noted that partial re-infiltration occurs from surface runoff if the local slope of the grid-cell is ≤0.5% (D’Orgeval et al., 2008). Each grid box has a unique soil texture and structure (Post and Zobler, 2000), but three different soil columns are considered, each one with its own soil moisture discretization and root profile. These are classified as: bare soil, low and high vegetation regrouping the 13 Plant Functional Types (PFT) defined in ORCHIDEE. These PFTs contribute to the soil layers of each grouping a root density to compute extraction and soil moisture stress to the plants. The water balance is solved for each soil column resulting in three different soil moisture profiles in each grid box.

ORCHIDEE's soil temperature profile is calculated solving the heat diffusion equation. Contrary to the hydrological scheme, it considers a 7 layer discretization, where the layers' thicknesses follow a geometric series of ratio 2, and a total soil depth of 5.5 m (Hourdin, 1992; Wang et al., 2016). For this study, the first 2 m of the temperature profile were calculated following the same soil discretization as the one considered in the soil moisture calculation. The energy balance takes into account the skin temperature as presented in Schulz et al. (2001) to derive the Land Surface Temperature (LST). The soil and vegetation are considered as a single medium assigned with a surface temperature (Santaren et al., 2007).

H-TESSEL

The H-TESSEL LSM (Balsamo et al., 2009), developed by the ECMWF, revises and improves certain aspects regarding the soil hydrology of the TESSEL model. Its hydrology scheme solves a diffusive equation over a multilayer scheme with a 4 layer discretization. Layer depths follow an approximate geometric relation (Table 1). In addition, the soil can be covered by a single snow layer. H-TESSEL considers the same lower boundary condition as ORCHIDEE. However, it differs in the upper one that accounts also for infiltration. It defines a maximum infiltration rate given by the maximum downward diffusion from the saturated surface. Once this rate is exceeded by the water flux at the surface, the excess of water is derived to surface runoff.

The model considers six types of tiles over land: bare soil, low and high vegetation, water intercepted by leaves, as well as shaded and exposed snow. Each one of these has its own energy and water balance. However, only one soil moisture reservoir is considered. Recent improvements have replaced a globally uniform soil type (loamy) by a spatially varying one (coarse, medium, medium-fine, fine, very fine, organic). Surface runoff, based on variable infiltration capacity, was also a recent improvement.

H-TESSEL's soil temperature profile is computed using the same soil discretization as the one defined in its hydrological scheme. The soil heat budget follows a Fourier diffusion law, which has been modified to consider also thermal effects caused by changes in the soil water phases (Holmes et al., 2012). To simulate the LST, a skin layer is defined representing i) the layer of vegetation, ii) the top layer of bare soil, or iii) the top layer of the snow pack. The surface energy balance equation is then linearised for each tile (Viterbo and Beljaars, 1995).

Both LSMs are forced with the ERA-Interim forcing (Dee et al. 2011), which is suitable for this study because it ranges from 1979 to 2012 and recent data were needed to perform the comparison with SMOS's. We are aware that biases in this kind of forcings have an effect on the LSMs simulations (Ngo-Duc et al., 2005). ORCHIDEE was configured to output hourly TB values. However, TB_{HT} is only available at 6 hourly time steps (at 00, 06, 12, and 18 hours). Due to this difference, each set of modelled TBs was sampled in a different way to approximate TB_{SM} measurement times. The sampling processes will be explained in Section 3.

The above paragraphs show that the hydrology, soil processes and land surface temperatures are approached very differently by both models. Therefore, the impact of these differences needs to be considered when comparing simulated TBs.

2.3 Precipitation and Land Surface Temperature

One important common feature of the presented model simulations is the forcing data. Since biases in the imposed atmospheric conditions can affect modelled TBs, it was decided to validate two important variables for which independent observations exist. Focus was put on Precipitation (P) and the Land Surface Temperature (LST), as they are key variables for the water and radiative balances.

P is the main driver of SSM, and this directly drives the L-Band emissivity. According to Zollina et al. (2004), P generated by a reanalysis (like ERA-Interim which is used here) is highly model dependent and it should be noted that models do not represent accurately all the physical processes of the atmospheric water cycle. Therefore, the verification of this forcing variable of the LSMs with independent data is essential.

As for the radiative balance, the available energy at the surface is one of the major drivers of LST. We chose to verify this variable in this study for two reasons. First, it provides a good summary of the surface energy balance. Second, it is a key parameter in CMEM's estimation of TB. Therefore, its analysis will indicate whether the LSM thermodynamics shows biases with spatio-temporal characteristics similar to those from TBs.

The independent datasets used for validation are:

- P from the E-OBS dataset (Haylock et al., 2008),
- LST provided by the LandSAF product (http:// landsaf.meteo.pt).

It should be noted that these products have errors which must be taken into account when used. For example, E-OBS data can be over-smoothed depending on the station network density (Hofstra et al., 2009) or for LST sensor noise, emissivity uncertainties, etc. are error sources which can propagate in the LandSAf algorithm (Freitas et el., 2007). However, these products are accepted by the community to be representative of large spatial scales and we have selected them as the reference to benchmark P and LST.

3 Methods

3.1 Data sampling and filtering processes

To compare modelled and measured brightness temperatures, TB_{OR} and TB_{HT} were sampled with TB_{SM} and remapped to the nearest neighbour of the SMOS grid. This allows to keep the spatial structures of the coarse model resolution. Next, the three TB signals were filtered to exclude certain situations, such as frozen soils or RFIs, which are known to make SSM estimates unreliable.

3.1.1 Sampling

The objective of sampling the data is to use only modelled TBs corresponding to available measured values. TB_{OR} were sampled at an hourly scale. However, TB_{HT} consists of 6 hourly values, thus potentially resulting in a large number of neglected data because TB_{HT} and SMOS time steps did not always correspond. Therefore, TB_{HT} were sampled considering a 3 hour window around the observation in order to keep a larger number of modelled data for the comparison. To test the impact of this approximation, we also applied it to the TB_{OR} and compared it to the original hourly data. Differences between them were under 0.1% for the diagnostics used here, and thus, it was considered to be negligible.

3.1.2 Filtering

Data was filtered to discard unreasonable TB values from the comparison study. Filtering rules were devised following the ECMWF criteria used to screen TB_{HT} (Table 3). Common filters were also applied to measured and modelled TBs.

The filters applied in TB_{HT} corresponding to the water content in snow cover (snow water equivalent) and the criterion on ERA-Interim's 2 m air temperature aim to discard frozen soils, which might affect the SM retrieval (Dente et al., 2012). The same result was achieved by filtering TB_{OR} with the 2 m temperature from the forcing (as in the previous case) as well as with ORCHIDEE's average surface temperature. The first common criterion excludes TBs higher than 300 K to avoid effects of RFIs, which can result in overestimated brightness temperatures (can be higher than 1000 K). The second common criterion aims at removing points which might be influenced by coastal or topographic effects, as does H-TESSEL's orography (slope) criterion too. The mask was built using the L2 SMOS product. Any pixel with no surface soil moisture data retrieved was excluded from the comparison. The surrounding 24 pixels were also excluded to avoid effects of abrupt changes in land/sea transitions. In the end, only data which is not masked in either case is retained.

3.2 Comparison analyses

3.2.1 Spatio-temporal correlation

The first diagnostic performed to compare measured and modelled TBs consisted in temporal and spatial correlation analyses. Our aim was to study the similarity between the spatio-temporal patterns. We used the Pearson product-moment correlation coefficient. Only values statistically significant at the 95% level were considered. An averaging window of 5 days was applied to the data before performing spatial correlation analysis to ensure the highest coverage possible.

Even though the correlation coefficient is a widely used statistical tool, it may not be suitable when analysing certain fields. For instance, Polcher et al. (2016) show that temporal correlation measured between remotely sensed, in-situ, and modelled SSM, is mainly driven by the high frequency behaviour of SSM. Therefore, this diagnostic is not very sensitive to the slower variations of the field studied. Performing the correlation analyses allowed us to study if this conclusion also applies to TBs.

3.2.2 Empirical Orthogonal Function

The Empirical Orthogonal Function (EOF) analysis extracts the dominant spatial and temporal modes of variability of a field (F). It relates the spatial patterns of each variation mode with a time series and its explained variance.

To do so, the covariance matrix (R) of F is computed. Next, the eigenvalue problem is solved:

$$RC = C\Lambda \qquad (1)$$

Where Λ is a diagonal matrix that contains R's eigenvalues (Λi) and C is a matrix where its column vectors (ci) are R's eigenvectors, which correspond to Λi.

Each eigenvalue corresponds to a variability mode and provides a measure of the total variance in R explained by the mode. Therefore, the biggest eigenvalue will correspond to the dominant variability mode. The eigenvector ci is the spatial pattern (Pi) of the mode of variation i. The temporal evolution of a mode of variation is obtained by projecting the field F on the corresponding spatial pattern:

$$\vec{\alpha j} = F \vec{cj} \qquad (2)$$

We will refer to these temporal series as the Expansion Coefficients (ECs). Positive values of ECs imply that there is no sign change in the spatial patterns. The EOF methodology is detailed in Björnsson and Venegas, (1997).

We applied the EOF analysis to the error between measured and modelled TBs, to characterize it spatially and temporally. Identifying the main modes of variability of an error field allows proposing and testing hypotheses about its causes. We followed this approach to analyse the impact of forcing biases on modelled TBs. Other studies have also applied this methodology to error analysis. For example, Kanamitsu et al. (2010) analyze the impact of a regional model error on the inter-annual variability of a set of analysis fields.

4 Results

The temporal evolution and spatial structures of measured and modelled TBs are analyzed in this section. This study follows the comparison between modelled and retrieved SSM (Polcher et al., 2016) and attempts to elucidate if the difference found can be attributed either to the retrieval algorithm, which converts TBs into estimated SSM, or its modelled counterpart.

4.1 Comparison of modelled and measured TBs

The mean temporal and spatial correlations between measured and modelled TBs, over the IP from 2010 to 2012, are shown in Table 4. Values from the SSM comparison performed by Polcher et al. (2016) are also included. The differences between spatial and temporal correlation are already apparent and warrant separate analyses as a first step.

4.1.1 Temporal correlation

Fig. 1 shows the temporal correlation between measured and modelled daily TBs for the horizontal and vertical polarizations. Both polarizations show a good agreement between models and observations in their temporal evolution, with values above 0.7 over a large part of the IP. This can be explained by the strong annual cycle imposed by the surface temperature, but more important are the quick responses of temperature and emissivity to precipitation events, which drive TB's fast variations and correspond to the synoptic variability of the signal. The high correlations indicate that it is well captured by both models. It confirms our hypothesis (Section 3.2.1) that the temporal correlation of TB is driven by the synoptic variability, as demonstrated in the SSM comparison performed by Polcher et al. (2016). Most of the areas with lower correlations correspond to mountain ranges. Relief effects on MW radiometry over land (Mätzler and Standley, 2000) are a difficult remote sensing problem and thus, discrepancies are expected. In fact, the lowest correlations (0.3 to 0.6) appear over some areas of the Pyrenees. Other examples are the Iberian System and the Cantabrian Mountains, located over the northeastern and the northern regions of the peninsula, respectively.

There are no large differences between the temporal correlation maps of TB_{OR} and TB_{HT} with TB_{SM} (Fig. 1). Since the same forcing was used, the two LSMs share the same synoptic variability from the ERA-Interim reanalysis. However, Fig. 1 shows that the synoptic variability of H-TESSEL leads to slightly higher correlation values than ORCHIDEE's, especially over the northern part of the IP.

4.1.2 Spatial correlation

For clarity, the 5 daily spatial correlations are averaged per season and the distribution of values obtained is represented in a boxplot form in Fig. 2. In general, the correlation is poor throughout the year. Although maxima are around 0.6, the annual mean ranges between 0.2 and 0.3 (Table 4). This implies that the spatial structures from both modelled TBs are not consistent with those observed by SMOS. We would like to point out the seasonality in the correlation. The lowest correlations occur during winter, where even negative values are obtained. These improve during spring and summer, and weaken again in fall. Moreover, winter and fall generally show larger ranges of variability and thus, a wider dispersion of the data than spring and summer. Fig. 2 also shows that the vertical polarization has systematically higher mean correlations than the horizontal one, except for the winter season. Finally, there is no significant difference in the correlation of TB_{SM} with either modelled TB as has already been noted for the temporal correlation.

4.2 Spatial and temporal characterization of the TB error

The spatio-temporal variability of the error between modelled and measured TBs is studied to better understand the poor consistency of their spatial structures. We want to analyse if this difference can be related to some physical process which might be incorrectly represented in both models. For this, an EOF analysis of the TB errors (TB_{OR} - TB_{SM} and TB_{HT} - TB_{SM}) is carried out.

4.2.1 TB error

Spatial patterns

Fig. 3 shows the spatial patterns of the first two EOF variation modes correspondent to the TB error of ORCHIDEE (TB_{OR} – TB_{SM}), for the horizontal and the vertical polarizations. The variance explained by each mode is also provided as a percentage in brackets. The total variance explained by the patterns of the first variation mode is above 30% in both polarizations: 36% (horizontal) and 31% (vertical). These two patterns show a similar structure characterised by high values over the southwest and a smaller area further north of the IP, which weaken as they extend through the rest of the peninsula. This similarity is confirmed by their high spatial correlation, which is 0.99 (Table 5). The second variation mode exhibits a structure that is also maximum over the southwest of the IP in both polarizations. However, the total variance explained has decreased to 6% and 7% (horizontal and vertical polarization, respectively).

Fig. 4 is equivalent to Fig. 3 but presents the TB error of H-TESSEL (TB_{HT} – TB_{SM}). The variance fractions explained by the first EOF mode are 30% and 18% for the horizontal and vertical polarization, which are lower than those obtained for the TB error of ORCHIDEE. As in Fig. 3, the first variation modes show similar spatial structures, which are highly spatially correlated (0.86, Table 5). It is interesting to note that this structure coincides with the one identified for the TB error of ORCHIDEE (Fig. 3 a and c). This is confirmed by the high correlation obtained between the patterns of the two errors: 0.92 and 0.73 for the horizontal and vertical polarization, respectively (Table 5). The second variation mode of H-TESSEL's

TB error explains 8% (horizontal polarization) and 12% (vertical polarization). The horizontal polarization pattern shows that the error is maximum over the southwestern region of the IP, while the vertical polarization pattern does not show a clear structure. Contrary to the first variation mode, patterns from the second one show larger differences with the patterns depicted by the TB error of ORCHIDEE.

Expansion coefficients

Fig. 5 shows the ECs of the first EOF variation mode of both TB errors. In other words, the projection of the error time series on the EOF pattern, summarizing how much the error field varies according to the pattern.

The four series show a strong annual variation which peaks in fall. High values are also observed in December 2012 and during the winter 2010 - 2011. It should be noted that the behaviour of the ECs coincides with the marked seasonality shown in Fig. 2 and thus, reinforces our observation that modelled TB patterns have their strongest disagreement with SMOS measurements in fall and winter. The ECs of the second EOF variation mode of each TB error have not been included in Fig. 5, because the spatial patterns of each error differ between them. Nevertheless, it is important to note that they show variations at higher frequency than those from the first mode.

Two conclusions can be drawn from these results:

First, the largest spatially coherent error identified in Fig. 3 and 4 (a and c) is dominated by the slow varying component of the TB signals, which is driven by the annual cycle. At first sight, this might seem to contradict the temporal correlation analysis (Fig. 1). However, it evidences that the slow (annual cycle) and fast (synoptic variability) components of TBs show different behaviours.

Second, modelled TBs are warmer than measured ones over southwestern IP during fall and winter, revealed by the first EOF patterns and their oscillations (Fig. 3 to 5). To further analyze this result, we looked at ECMWF's mean error from the months of November 2010 to 2012. This diagnostic consists of the time averaged geographical mean of the difference between SMOS measured TBs and modelled ones using the CMEM and H-TESSEL's surface state variables (Fig. 6). For all three years we see a contrast between the error over the northwestern region of the IP (in an orange colour) and over the southwestern region and a smaller area further north (in a blue colour). According to this, measured TBs are warmer than modelled ones over the northwest of the IP during these three periods, while modelled TBs are warmer than SMOS's over the southwest of the IP. This is in good agreement with the behaviour described by the first EOF variation mode of both TB errors (Fig. 3 and 4, a and c). It should be noted that the mean error shows a global bias between the spatial patterns of measured and modelled TBs. However, only the IP is represented in this figure to show clearly the spatial structures.

To summarize, the EOF analyses of the ORCHIDEE and H-TESSEL TB errors identified a common dominant structure, which is maximum in the fall and winter seasons, over the southwest of the IP and a smaller area further north. It represents between 18% and 36% of the error depending on the modelled TB set considered and its polarization. Moreover, it corresponds well with the ECMWF mean error for the 2010-2012 November months.

4.2.2 LST and Precipitation errors

Precipitation and LST data are used to explore possible causes for the difference between measured and modelled TBs. Errors are calculated with respect to independent datasets. The dominant error pattern of each variable is computed via EOF analysis and compared with the dominant pattern of the ORCHIDEE and H-TESSEL TB errors. If similarities can be identified, then possible causal links between these variables and the TB error can be explored.

The precipitation error is calculated as the difference between the P provided by the ERA-Interim forcing and the E-OBS independent dataset. The LST errors are computed as the difference between modelled LST (from ORCHIDEE or H-TESSEL) and the EUMETSAT LandSAF product (http://landsaf.meteo.pt).

Spatial patterns

The first EOF patterns of P and LST errors are represented in Fig. 7, together with their explained variance. The precipitation error is common to both models as it originates in the selected forcing. The dominant spatial structure of this error, which represents only 15% of the total variance, has its maximum in the southeast of the IP and is different from the one found for TB. The error patterns from LST differ remarkably between the two models and do not seem related to the TB error. On the one hand, a North-South gradient is observed in ORCHIDEE's LST error (Fig. 7 a), which is most likely explained by forcing induced biases due to available energy affecting the LSM simulation. On the other hand, H-TESSEL's LST error pattern (Fig. 7 c) shows a gradient from East to West.

Expansion coefficients

The ECs correspondent to each of these patterns are presented in Fig. 8. Those for the precipitation error show a higher frequency variation than those of the LST and TB errors. ORCHIDEE's LST error behaves as expected from land-surface physics, with a maximum in summer when the largest amount of energy is absorbed by the surface and thus, small errors in the energy balance translate into large temperature differences. This is not the case for H-TESSEL's LST error, whose ECs show higher frequency variation with maxima in the fall season and at the end of the winter in 2011 and 2012.

The dominant modes of variability of P and LST errors show different spatial and temporal characteristics than the TB error dominant pattern. Neither the spatial structures coincide, nor their temporal evolution over the 2010 to 2012 period. The TB errors show a strong annual variation which peaks in fall and winter. The ECs of ORCHIDEE's LST error show a maximum in summer, while those for H-TESSEL's LST and P errors are characterized by higher frequency variations.

The difference between the EOF analyses' results of P, LST, and TB errors suggest that their error sources differ. Therefore, even though the products taken as reference (E-OBS and LandSAF) are affected by errors, these do not seem to be responsible for the dominant mode of the TB discrepancy. The EOF analysis excludes the hypothesis that biases in precipitation driving the models or errors in their surface temperature are the direct cause of the inconsistency in TB's spatial structures. The strong similarity of the TB errors in two quite different LSMs further strengthens the rejection of this hypothesis.

4.2.3 Analysis of CMEM assumptions

The CMEM is another candidate to explain the TB error since it is also a common element from both sets of modelled TBs. In fact, modelled TBs have been shown to be more sensitive to the configuration of the microwave model than to the LSM used (de Rosnay et al., 2009).

As explained in section 2, we performed a sensitivity analysis to test if certain CMEM parameterizations could explain the differences between measured and modelled TBs. As a result, three new sets of modelled TBs were estimated: $TB_{HT(VC)}$, $TB_{OR(SD)}$, and $TB_{OR(FW)}$ to evaluate the role of vegetation, vertical discretization, and the emissivity parameterization respectively.

In the first place, $TB_{HT(VC)}$ shows similar mean spatial correlations with TB_{SM} as the ones for TB_{HT} and TB_{SM} (Table 4). In addition, an EOF analysis of the difference between this new estimate and observed TBs (figure not included) shows similar spatial patterns as the ones identified in Fig. 4 (a and c), as well as a good agreement between their ECs.

In the second place, no significant differences were observed between $TB_{OR(SD)}$ and TB_{OR} when compared to TB_{SM}. For instance, mean spatial correlations computed using $TB_{OR(SD)}$ and TB_{SM} are 0.22 and 0.33 for the horizontal and vertical polarization, which are similar to the values obtained for TB_{OR} and TB_{SM} (Table 4).

In the third place, an EOF analysis of the TB error computed using the $TB_{OR(FW)}$ and the TB_{SM} sets (figure not included), shows a similar dominant structure both in space and time to the one observed in Fig. 3 (a and c). In addition, similar spatial correlations between $TB_{OR(FW)}$ and the TB_{SM} to those from TB_{OR} and TB_{SM} are also found (Table 4).

As synthesized in Table 4, in the current state of CMEM the vegetation cover, the number of soil layers, and the ε_s and T_{eff} parameterizations can be discarded as the dominant factors responsible for the poor spatial correlation between modelled and SMOS TBs.

4.3 Annual cycle of TBs

The slow varying component of the TB signals is analyzed pixel by pixel, because it has been identified as the driver of the largest spatially coherent error structure between measured and modelled TBs (Fig. 5). For this matter, the mean annual cycle of each TB signal was computed for each pixel and then smoothed using a spline filter to remove sub-monthly fluctuations. The period of study is too short to ensure that a simple annual mean cycle filters out high frequency variations. In Fig. 9 the normalized amplitudes of the annual TB cycle are displayed.

The spatial structures shown in SMOS's maps (Fig. 9, c and f) exhibit strong resemblances to those observed in the first EOF patterns of the TB error (Fig. 3 and 4, a and c). However, this structure is not found in the maps corresponding to TB_{OR} and TB_{HT}, where there is less contrast in the spatial distribution of the relative amplitude of the annual cycle. This indicates that the LSMs combined with CMEM do not reproduce the annual cycle amplitude of TBs observed by SMOS.

To further analyse this result, two study areas are defined (Fig.10). The first one is over the southwestern IP (7.5W : 4W, 40N : 38N) and corresponds to part of the area where the largest differences in TB’s normalized amplitudes are identified. The second one is the northwestern region (8.25W : 6W, 43N : 41.75N) of the IP and is chosen because it shows similar annual cycle amplitudes of TB in the two models and SMOS. In addition, the EOF analysis of the TB error showed opposite behaviours in these areas.

Fig. 10 shows the smoothed annual cycle of the horizontal and vertical polarizations of the TB signals from both regions. The LST from the LandSAF product as well as those modelled by ORCHIDEE and H-TESSEL are also displayed because of their direct relation to TBs. The plots show that the TB's annual cycle behaviour differs between the both regions and are not related to the LST errors obtained when comparing to the LandSAf product. Therefore, the processes responsible for the TB error are probably different in each one of them.

The following results can be extracted from the plot corresponding to the southwestern area (Fig. 10 a):

In winter, the difference between models is small compared to their relative warm bias when compared to SMOS. In summer, the agreement is relatively good with observations laying within the spread of the models. This explains the result presented above, namely that the amplitude of the simulated annual cycle is smaller than for the remotely sensed TB. Examining the LST one can note that the biases are relatively small and ORCHIDEE generally matches better the LandSAF product, but H-TESSEL shows a larger and more correct amplitude of the annual cycle. This might explain why this model has the largest amplitude of TB in both polarisations, indicating that a large fraction of the error on the annual cycle of TB is caused by the emissivity simulated by CMEM given the surface states of both LSMs.

Over the northwestern IP, SMOS observations are mostly within the uncertainty spanned by the two models. One notable exception is the summer period for the horizontal polarization where both models are cooler. Also in this region the amplitude of TB in both polarizations is larger in H-TESSEL than ORCHIDEE and closer to that measured by SMOS. Again, this can be related to LST. Although ORCHIDEE has smaller biases, the H-TESSEL amplitude of the annual cycle is larger and closer to the observed one.

The strong difference in behaviour between the two selected regions in winter is already visible in the dominant EOF mode of the TB errors. The spatial patterns (Figures 3 and 4) have different signs in the northwestern and southwestern regions. For both regions, the LST biases of the LSMs do not show a clear relation to the simulated TBs. H-TESSEL has the warmest surface temperatures but the lowest TBs, indicating that its state variables produce a lower emissivity than ORCHIDEE when processed by CMEM. On the other hand, the differences in annual amplitudes of LST could contribute to the differences in the amplitude of the simulated TB annual cycle. This is also supported by the fact that the dominant variation modes of LST errors are not related to those of TBs. This would indicate that the major contribution to the TB errors found for the models does not originate in their forcing or their ability to simulate the land surface energy balance and temperature, but rather in the way CMEM simulates L-band emissivity based on their description of the surface state.

5 Discussion

This work complements with an analysis of TBs the study by Polcher et al. (2016), which compared the SSM product of SMOS with ORCHIDEE's modelled SSM. Both studies present a spatio-temporal correlation analysis and obtain similar results: a good agreement in temporal evolutions and a large mismatch between the spatial structures of measured and modelled SSM and TB.

The temporal correlation between TB_{OR} and TB_{SM} is very similar to that between retrieved (SMOS) and modelled (ORCHIDEE) SSM (Table 4). In addition, both variables show lower correlations over mountain ranges. As noted for SSM, the temporal correlation is mainly driven by its fast varying component and is not very sensitive to the annual cycle (Polcher et al., 2016).

Spatial correlations are low for both variables, indicating an inconsistency between the spatial structures of measured and modelled data. Polcher et al. (2016) showed that the spatial correlation between retrieved and modelled SSM is worse for the SSM's slow varying component than for its fast varying component. This can be due to the fact that the largest spatially coherent error between measured and modelled TBs is dominated by their slow varying component, as shown in this paper.

The EOF analysis presented here identified a dominant structure over the southwestern IP using both sets of modelled TBs, which explains a large fraction of the TB error. This structure differs from the error characterization of the SSM comparison, which showed the largest discrepancies between modelled and retrieved SSM over the northwestern IP. In fact, only weak differences were found for SSM over the southwestern region (Polcher et al., 2016). These results indicate that the transfer functions used by SMOS to derive SSM from observed TBs or CMEM, which estimates TBs from modelled SSM (together with other state variables), play an important role and have to be better understood in order to explain the differences between the SMOS observations and the simulated surface states.

None of the hypotheses tested to identify a methodological weakness in the forcing of both LSMs or the configuration of CMEM, which would explain this common error, was conclusive. The differences in TB between the LSMs and SMOS are noteworthy and we believe that understanding them should be a priority for the community to achieve a better usage of these observations. As the LSMs used here are very different in their conception, it is unlikely that they produce the same systematic SSM bias which would explain the large discrepancy in the southwest of the IP during winter. On the other hand, processes which are not represented with enough detail in both schemes could explain the error and need to be analyzed as to their potential to explain the discrepancies.

- In the first place, it is interesting to study the Leaf Area Index (LAI), because it is linked to the seasonal cycle of vegetation. It may, therefore, reveal some underestimated effects of vegetation dynamics on modelled TBs, which could be related, to a certain extent, to the seasonality identified in the dominant structure of the TB error. In addition, the LAI is a key component in the CMEM parameterization of τ_{veg}. However, the areas of the IP where the TB error is the largest are those of least vegetation. Therefore, in our opinion, modelled LAI is not likely to be the main cause of the differences in TB’s spatial structures.
- In second place, assumptions made in the modelling of rainfall interception may also explain some differences between modelled and measured TBs. In particular, those shown in Fig. 10 (b) over the northwestern region of the IP. This region is characterized by an oceanic climate and thus, wet winters and mild summers, with a high precipitation, and often rainfall occurring as drizzle. Contrary to the southern region, there is more vegetation and thus, rainfall interception plays a key role over this area and may be of interest to revise how this process is modelled. However, the IP region with strong interception is not the one with the largest TB error. The error

over the southwestern region is larger than over the northwestern region, as shown by the EOF analysis.

- In third place, the attenuation effect of litter on the soil and its interception of water could also explain differences obtained between modelled and measured TBs, since it is not taken into account by models, but is part of satellite observations. However, we believe that probably it would not cause an impact structured as the one observed over the southwestern area of the IP without affecting other regions. Indeed this process would be strongest in regions with dense vegetation.
- Finally, issues related to the fundamental simplification of subgrid processes in LSMs may also contribute to the inconsistency between the spatial structures of modelled and measured TBs. For instance, LSMs do not represent small scale features as open water in lakes and rivers, swamps, irrigated areas or other water ponded on the surface and could contribute strongly to L-band emissivity of the surface. Assumptions made by LSMs could neglect key issues from the small scale which could be carried over to the large scale of TBs. For the moment, we do not see why these simplifications of LSMs would have the strongest impact in the southwest of the IP.

Instrumental issues from SMOS could also explain the differences in TB spatial structures, in case these are not of climatological or geophysical nature. For example, one of the most important causes of noise in SMOS surface soil moisture is Radio-Frequency Interferences (RFIs). Daganzo-Eusebio et al. (2013) describe their effect on SMOS data. Some of them are difficult to detect and thus, RFIs may not be properly filtered out. For instance, Dente et al. (2012) identified an irregular angular pattern in the TBs affecting data from the L1C product used to retrieve soil moisture. In their opinion, this was caused by weak RFIs which were not correctly filtered. Another explanation could be antenna pattern errors, as SMOS TBs seasonal and latitudinal drifts detailed in Oliva et al. (2013). However, RFIs are not likely to be the main cause of the differences between measured and modelled TBs, because the main spatial structure identified in both TB errors is found to be dominated by the brightness temperature's annual cycle. This suggests that it contains a geophysical signal.

In our opinion, further analyses should be carried out regarding the CMEM assumptions concerning emissivity. According to Jones et al. (2004), the soil moisture and vegetation water content have a significant effect on the sensitivity of TB at the top of the atmosphere. However, they impact microwave emission in different ways. On the one hand, an increase in soil moisture results in a higher soil dielectric constant (Є) and thus, on lower emissivities. On the other hand, an increase in the vegetation water content rises the scatter and the absorption, increasing the emission. The Є is key in the computation of emissivity, while the vegetation optical depth (τ_{veg}) is closely related to the vegetation water content. Both variables are modelled in CMEM and the same parameterization has been used to estimate the two sets of modelled TBs: Wang and Schmugge (1980) for Є and Wigneron et al. (2007) for τ_{veg}. Furthermore, the same parameterization has been used to model the rough surface emissivity (ε_r) in both cases: Wigneron et al., 2001. Considering that similar spatial patterns were obtained for the TB error using two different LSMs, focus should be put on the above mentioned variables (Є, τ_{veg}, and ε_r) in CMEM. We suggest to prioritize the analysis of the relation between the vegetation water content and TB because of the role the vegetation opacity model plays in CMEM's configuration, as shown in de Rosnay et al. (2009). In addition, no significant differences were observed between modelled and retrieved SSM over southwestern IP (Polcher et al. 2016), where the maximum TB error was identified. This reassures our suggestion of prioritizing τ_{veg} with respect to Є, since the latter is directly related to SSM.

The hypotheses analyzed to identify the cause of TB's error dominant mode, as well as those proposed to study it, are listed in Table 6. The conclusion obtained for each analysis is also included.

6 Conclusions

TBs of SMOS Level 1C product were compared to two sets of modelled TBs. The latter were obtained using simulated state variables (from the ORCHIDEE and H-TESSEL LSMs) and a radiative transfer model, CMEM. The study was carried out over the Iberian Peninsula (IP) for the period 2010 to 2012.

On the one hand, a temporal correlation analysis between measured and modelled data shows that there is a good agreement in their temporal evolution. However, this diagnostic is mainly driven by the TB's signal synoptic variability, as occurs with SSM (Polcher et al., 2016). On the other hand, a spatial correlation analysis detected a large mismatch between the TB spatial structures provided by models and observations.

An EOF analysis of the error between modelled and measured TBs suggests that the inconsistency is not limited to a particular LSM. It is dominated by the TB slow varying component, peaking in fall and winter. In addition, modelled TBs are larger than SMOS measurements during these seasons over the dominant error structure detected. This structure explains between 18% and 36% of the TB error variance, depending on the LSM and polarization. Therefore, there is a high percentage of the error (between 82% and 64%) that shows structures which have to be analyzed and explained. Since these are not present in both LSMs, they are of lower priority and have not been approached in this study.

Forcing induced biases are discarded as the main cause of the spatial inconsistency in TBs after computing the dominant error structures of precipitation and Land Surface Temperature (LST). Nevertheless, the degree of accuracy of the forcing cannot be fully established because of scale issues and the lack of sufficient independent measurements. The difference in TBs' spatial structures could also be thought of a combination of non linear relations between errors in precipitation and LST, but this is beyond the scope of this paper.

Assumptions made in certain CMEM parameterizations are also discarded as the main source of the spatial inconsistency between measured and modelled TBs: the vegetation cover input; the number of soil layers defined; and some parameterizations to compute the smooth surface emissivity (Fresnel law and Wilheit (1978)) and the effective temperature (Wigneron et al. (2001) and the temperature profile).

Previous studies found differences between the spatial structures of modelled and retrieved SSM (Parrens et al., 2012; Polcher et al., 2016). This paper shows that these structures are not consistent also when comparing modelled and observed TBs. In addition, this issue is amplified for the TBs compared to SSM, because the latter are bounded by zero and saturation. This could explain the generally better spatial correlation for SSM in winter, when it reaches saturation in large parts of the IP. Although this study is limited to the IP, differences in spatial structures occur at a global scale. We would like to draw the reader's attention to the fact that TBs are not only the main input of SMOS soil moisture retrieval algorithm, but that they are used to retrieve other variables, like vegetation optical depth or salinity. We believe that analysing the spatial inconsistencies between modelled and measured TBs is important, as these can affect the estimation of geophysical variables, TB assimilation in operational models, as well as result in misleading validation studies. Therefore, obtaining the spatial contrast of measured TBs in models is a challenge which, in our opinion, deserves a higher priority in the community.

Acknowledgements

The authors would like to thank Filipe Aires and Jean-Pierre Wigneron for their helpful comments. We are also very thankful to one anonymous reviewer who’s comments have greatly improved the document. This work contributes to the FP7 Earth2Observe project under grant agreement No 603608.

References

Albergel, C., Zakharova, E., Calvet, J. C., Zribi, M., Pardé, M., Wigneron, J. P., Novello, N., Kerr, Y., Mialon, A., and Fritz, N.: A first assessment of the SMOS data in southwestern France using in situ and airborne soil moisture estimates: The CAROLS airborne campaign, Remote Sens. Environ., vol. 115, no. 10, pp. 2718–2728, 2011.

Balsamo, G., Vitterbo, P., Beljaars, A., van den Hurk, B., Hirschi, M., Betts, A. K., and Scipal, K.: A Revised Hydrology for the ECMWF Model: Verification from Field Site to Terrestrial Water Storage and Impact in the Integrated Forecast System, J. Hydrometeor., 10, 623-643, DOI:10.1175/2008JHM1068.1, 2009.

Baroni G., Facchi A., Gandolfi C., and Ortuani B.: Analysis of the performances of methods for the evaluation of soil hydraulic parameters and of their application in two hydrological models. In : Santini A. (ed.), Lamaddalena N. (ed.), Severino G. (ed.), Palladino M. (ed.). Irrigation in Mediterranean agriculture: challenges and innovation for the next decades. Bari : CIHEAM, 213- 222 (Options Méditerranéennes : Série A. Séminaires Méditerranéens; n. 84) , 2008.

Bircher, S. and Kerr, Y.: Validation of SMOS L1C and L2 Products and Important Parameters of the Retrieval Algorithm in the Skjern River Catchment, Western Denmark, IEEE Trans. Geosc. Rem. Sens., 51, 5, 2013.

Björnsson, H., and Venegas, S. A.: A Manual for EOF and SVD Analyses of Climate Data. Report No 97-1, Department of Atmospheric and Oceanic Sciences and Centre for Climate and Global Change Research, McGill University, 52, 1997.

Bousseta, S., Balsamo, G., Beljaars, A., Kral, T., and Jarlan, L.: Impact of a satellite-derived leaf area index monthly climatology in a global numerical weather prediction model. International Journal of Remote Sensing 34, 9-10, 3520-3542, http://dx.doi.org/10.1080/01431161.2012.716543, 2013.

Cayan, D. R. and Georgakakos, K. P.: Hydroclimatology of continental watersheds. 2. Spatial analyses. Water Resources Research 31: doi: 10.1029/94WR02376. Issn: 0043-1397, 1995.

Daganzo-Eusebio, E., Oliva, R., Kerr, Y., Nieto, S., Richaume, P., and Mecklenburg, S.: SMOS radiometer in the 1400-1427-MHz passive band: Impact of the RFI environment and approach to its mitigation and cancellation, IEEE Trans. Geosci. Remote Sens., vol. 51, no. 10, pp. 4999–5007, 2013.

De Rosnay, P. and Polcher, J.: Improvements of the Representation of the Hydrological Exchanges between the Biosphere and the Atmosphere in a GCM, Hydrology and Earth System Sciences 2 (2-3): 239–56, 1998.

De Rosnay P., Drusch, M., Boone, A., Balsamo, G., Decharme, B., Harris, P., Kerr,Y., Pellarin, T., Polcher, J., and Wigneron, J. P.: The AMMA Land Surface Model Intercomparison Experiment coupled to the Community Microwave Emission Model: ALMIP-MEM", J. Geophys. Res., Vol 114, doi: 10.1029/2008JD010724, 2009.

Dee, D. P., Uppala, S. M., Simmons, A. J., Berrisford, P., Poli, P., Kobayashi, S., Andrae, U.: The ERA-Interim Reanalysis: Configuration and Performance of the Data Assimilation System, Quarterly Journal of the Royal Meteorological Society 137 (656): 553–97. doi:10.1002/qj.828, 2011.

Dente. L., Su, Z., and Wen, J.: Validation of SMOS Soil Moisture Products over the Maqu and Twente Regions. Sensors, 12, 9965-9986, doi:10.3390/s120809965, 2012.

D'Orgeval, T., Polcher, J., and de Rosnay, P.: Sensitivity of the West African hydrological cycle in ORCHIDEE to in- filtration processes, Hydrol. Earth Syst. Sci., 12, 1387–1401, doi:10.5194/hess-12-1387-2008, 2008.

Drusch, M., Wood, and Jackson, T.: Vegetative and atmospheric corrections for soil moisture retrieval from passive microwave remote sensing data: Results from the Southern Great Plains Hydrology Experiment 1997, J. Hydromet., 2, 181-192, 2001.

Entekhabi, D., Njoku, E. G., O'Neill, P. E., Kellogg, K. H., Crow, W. T., Edelstein, W. N., Entin, J. K., Goodman, S. D., Jackson, T. J., Johnson, J., Kimball, J., Piepmeier, J. R., Koster, R. D., Martin, N., McDonald, K. C., Moghaddam, M., Moran, S., Reichle, R., Shi, J. C., Spencer, M. W., Thurman, S. W., Tsang, L., and Van Zyl, J.: The Soil Moisture Active Passive (SMAP) Mission, Proceedings of the IEEE 98.5, 704-716, 2010.

Escorihuela, M. J., Chanzy, A., Wigneron, J. P., and Kerr. Y.: Effective Soil Moisture Sampling Depth of L-Band Radiometry: A Case Study. Remote Sensing of Environment 114 (5): 995–1001. doi:10.1016/j.rse.2009.12.011, 2010.

Freitas, S. C., Trigo, I. F., and Dias, J. B.: Error propagation in the LSA-SAF algorithm for Land Surface Temperature. Proceedings of the 2007 EUMETSAT Meteorological Satellite Conference, Amsterdam, The Netherlands, 24-28 September, 2007.

González-Zamora, A., Sánchez, N., Gumuzzio, A., Piles, M., Olmedo, E., and Martínez-Fernández, J.: Validation of SMOS L2 and L3 soil moisture products over the Duero Basin at different spatial scales. The International Archives of Photogrammetry, Remote Sensing and Spatial Information Sciences, XL-7/W3, 2015.

Green, W. H. and Ampt, G.: Studies on soil physics, 1. the flow of air and water through soils. J. Agric. Sci, 4(1) :1–24, 1911.

Haylock, M. R., Hofstra, N., Klein Tank, A. M. G., Klok, E. J., Jones, P. D., and New, M.: A European daily high-resolution gridded dataset of surface temperature and precipitation. J. Geophys. Res (Atmospheres), 113, D20119, doi:10.1029/2008JD10201, 2008.

Hofstra, N., New, M., and McSweeney, C.: The influence of interpolation and station network density on the distributions and trends of climate variables in gridded daily data. Clym.Dyn., 35, 841, doi:10.1007/s00382-009-0698-1, 2010.

Holmes, T. R. H., Jackson, T. J., Reichle, R. H., Basara, J .B.: An assessment of surface soil temperature products from numerical weather prediction models using ground-based measurements, Water Resources Research, 48 (2), p. W02531 http://dx.doi.org/10.1029/2011WR010538, 2012.

Hourdin, F.: Etude et simulation numérique de la circulation générale des atmosphères planétaires, PhD Thesis, available at: www.lmd.jussieu.fr/~hourdin/these.pdf, 1992.

Jones, A., Vukićević, T., and Vonder Haar, T.: A microwave satellite observational operator for variational data assimilation of soil moisture, J. Hydrometeor., 5, 213– 229, 2004.

Kanamitsu, M., Yoshimura, K., Yhang, Y. B., and Hong, S. Y.: Errors of Interannual Variability and Trend in Dynamical Downscaling of Reanalysis, J. Geophys. Res., 115, 17115, doi:10.1029/2009JDO13511, 2010.

Kerr, Y., Waldteufel, P., Wigneron, J. P., Delwart, S., Cabot, F., Boutin, J., Escorihuela, M., Font, J., Reul, N., Gruhier, C., Juglea, S., Drinkwater, M., Hahne, A., Martin-Neira, M., and Mecklenburg, S.: The SMOS mission: New tool for monitoring key elements of the global water cycle, Proc. IEEE, 98, 5, 666-687, 2010.

Kerr, Y., Waldteufel, P., Richaume, P., Wigneron, J. P., Ferrazzoli, P., Mahmoodi, A., Bitar, A. A., Cabot, F., Gruhier, C., Juglea, S., Leroux, D., Mialon, A., and Delwart, S.: The SMOS soil moisture retrieval algorithm, IEEE Trans. Geosci. Remote Sens, 50, 5, 1384-1403, 2012.

Kolassa, J., Aires. F., Polcher, J., Pringent, C., JimÃ©nez, C., and Pereira, J. M.: Soil moisture retrieval from multi-instrument observations: Information content analysis and retrieval methodology, J. Geophys. Res. Atmos., 118, 4847–4859, doi:10.1029/2012JD018150, 2013.

Krinner, G., N. Viovy, N., de Noblet-Ducoudré, N., Ogée, J., Polcher, J., Friedlingstein, P., Ciais, P., Stich, S., and I. C Prentice. 2005.: A Dynamic Global Vegetation Model for Studies of the Coupled Atmosphere-Biosphere System. Global Biogeochemical Cycles 19 (1). doi:10.1029/2003GB002199, 2005.

Le Vine, D., Lagerloef, G. S. E., and Torrusio, S.: Aquarius and remote sensing of sea surface salinity from space, P. IEEE , 98, 688–703, doi:10.1109/JPROC.2010.2040550, 2010.

Marthews, T. R., Quesada, C. A., Galbraith, D. R., Malhi, Y., Mullins, C. E., Hodnett, M. G., and Dharssi, I.: High-resolution hydraulic parameter maps for surface soils in tropical South America, Geosci. Model Dev., 7, 711-723, doi:10.5194/gmd-7-711-2014, 2014.

Mätzler, C., and Standley, A.: Technical Note: Relief Effects for Passive Microwave Remote Sensing. International Journal of Remote Sensing 21 (12): 2403–12, doi:10.1080/014311600050030538, 2000.

McMullan K., Brown, M., Martín-Neira, M., Rits, W., Ekholm, S., Marti, J., and Lemanczyck, J.:“SMOS: The payload”, IEEE Trans. Geosci. Remote Sens., 46, 3, 594–605, 2008.

Milly, P. C. D.: Potential evaporation and soil moisture in general circulation models, J. Climate, 5, 209–226, 1992.

Montzka, C., Bogena, H., Weihermüller, L., Jonard, F., Dimitrov, M., Bouzinac, C., Kainulainen, J., Balling, J. E., Vanderborght, J., and Vereecken, H.: Radiobrightness validation on different spatial scales during the SMOS validation campaign 2010 in the Rur catchment, Germany, IEEE Transactions on Geoscience and Remote Sensing, 51, 1728-1743, doi:10.1109/TGRS.2012.2206031, 2013.

Ngo-Duc, T., Polcher, J., and Laval, K.: A 53-Year Forcing Data Set for Land Surface Models, Journal of Geophysical Research 110 (D6). doi:10.1029/2004JD005434, 2005.

Oliva, R., Martín-Neira, M., Corbella, I., Torres, F., Kainulainen, J., Tenerelli, J., Cabot, F., and Martin-Porqueras, F.: SMOS calibration and instrument performance after one year in orbit, IEEE Trans. Geosci. Remote Sens., vol. 51, no. 1, pp. 654–670, 2013.

Parrens, M., Zakharova, E., Lafont, S., Calvet, J.-C., Kerr, Y., Wagner, W., and Wigneron, J.-P.: Comparing Soil Moisture Retrievals from SMOS and ASCAT over France, Hydrology and Earth System Sciences 16 (2): 423–40. doi:10.5194/hess-16-423-2012, 2012.

Parrens, M., Calvet, J.-C., de Rosnay, P., and Decharme, B.: Benchmarking of L-band soil microwave emission models, Remote Sensing of Environment, 140 pp 407-419, doi: 10.1016/j.rse.2013.09.017, 2014.

Pellarin, T., Wigneron, J. P., Calvet, J.-C., and Waldteufel, P.: Global soil moisture retrieval from a synthetic L-band brightness temperature data set, Journal of Geophysical Research (Atmospheres), 108, 4364, doi:10.1029/2002JD003086, 2003.

Polcher, J., Piles, M., Gelati, E., Tello, M., and Barella-Ortiz, A.: Comparing Upper-Soil moisture from SMOS and a land-surface model over the Iberian Peninsula, Remote Sens. Environ., Vol. 174, 69–81, doi:10.1016/j.rse.2015.12.004, 2016.

Post, W. M., and Zobler, L.: Global Soil Types, 0.5-Degree Grid (Modified Zobler). Available on-line [http://www.daac.ornl.gov] from Oak Ridge National Laboratory Distributed Active Archive Center, Oak Ridge, Tennessee, U.S.A., 2000

Rûdiger, C., Walker, J. P., Yann, K., Mialon, A., Merlin, O., and Kim, E. J.: Validation of the level 1c and level 2 SMOS products with airborne and ground-based observations, Proc. Int. Congr. MODSIM, Perth, Australia, Dec. 12-16, 2011.

Sánchez, N., Martínez-Fernández, J., Scaini, A., and Pérez-Gutiérrez, C.: Validation of the SMOS L2 Soil Moisture Data in the REMEDHUS Network (Spain). IEEE Transactions on Geoscience and Remote Sensing 50 (5): 1602–11, doi:10.1109/TGRS.2012.2186971, 2012.

Santaren D., Peylin P., Viovy N., Ciais P. : Optimizing a process-based ecosystem model with eddy-covariance flux measurements: a pine forest in southern France, Global Biogeochem. Cycles, 21, p. GB2013, 2007.

Schlenz. F., dall'Amico. T., Mauser, W., and Loew, A.: Analysis of SMOS brightness temperature and vegetation optical depth data with coupled land surface and radiative transfer models in Southern Germany, Hydrol. Earth Syst. Sci. Discuss., 9, 4, 5389-5436, 2012.

Schulz, J. P., Dümenil, L., and Polcher, J.: On the Land Surface–Atmosphere Coupling and Its Impact in a Single-Column Atmospheric Model, Journal of Applied Meteorology 40, 642-663, 2001.

Ulaby, F. T., Moore, R. K., and Fung, A. K.: Microwave Remote Sensing (Active and Passive), vol. 2. Reading, MA: Addison-Wesley, 1986.

Viterbo, P. and Beljaars, A.: An improved land surface parameterization scheme in the ECMWF model and its validation. Journal Climate, vol. 8, pp. 2716-2748, 1995.

Wang, F., Cheruy, F., and Dufresne, J.-L.: The improvement of soil thermodynamics and its effects on land surface meteorology in the IPSL climate model. Geosci. Model Dev., 9, 363–381, doi:10.5194/gmd-9-363-2016, 2016.

Wang, J. R., and Schmugge, T.: An empirical model for the complex dielectric permitivity of soils as a function of water content, IEE Trans. Geosc. Remote Sens., 18, 288-295, 1980.

Wigneron, J. P., Laguerre, L., and Kerr, H.: A Simple Parameterization of the L-band Microwave Emission from Rough Agricultural Soils, IEEE Trans. Geos. Remot. Sens., 39, 1697-1707, 2001.

Wigneron, J. P., Kerr, Y., Waldteufel, P., Saleh, K., Escorihuela, M., Richaume, P., Ferrazzoli, P., Grant, J. P., Hornbuckle, B., de Rosnay, P., Calvet, J.-C., Pellarin, T., Gurney, R., and Mätzler, C.: L-band microwave emission of the biosphere (L-MEB) model: Results from calibration against experimental data sets over crop fields, Remote Sens. Environ., 107, 4, 639–655, 2007.

Wilheit, T. T.: Radiative transfert in plane stratified dielectric, IEEE Trans. Geos. Remot. Sens., 16, 2, 138-143, 1978.

WWAP (World Water Assessment Programme): The United Nations World Water Development Report 4: Managing Water under Uncertainty and Risk, Paris, UNESCO, 2012.

Zollina, O., Kapala, A., Simmer, C., and Gulev, S. K.: Analysis of extreme precipitation over Europe from different reanalyses: a comparative assessment. Global and Planetary Change 44 129-161, 2004.

Table 1. CMEM configuration for the two sets of modelled TBs.

	Configuration	Parameterization	
		ORCHIDEE	H-TESSEL
Physical configuration	Soil dielectric constant	Wang and Schmugge (1980)	
	Effective temperature	Soil temperature profile	Wigneron et al. (2001)
	Smooth surface emissivity	Wilheit (1978)	Fresnel law
	Rough surface emissivity	Wigneron et al. (2001)	
	Vegetation optical depth	Wigneron et al. (2007)	
	Atmospheric optical depth	Pellarin et al. (2003)	
	Temperature of vegetation	Surface soil temperature	
	Vegetation cover input data	Ecoclimap	
Observing configuration	Microwave frequency	1.4Ghz	
	Incidence angle	42.5°	40°
Soil and atmospheric level configuration	Number of soil layers*	11	3
	(number of layers in the top 5 cm)	*(5)*	*(1)*

*Layer depths of ORCHIDEE's hydrological scheme [cm]: 0.099, 0.391, 0.978, 2.151, 4.497, 39.189, 18.570, 37.340, 74.880, 150, and 200

*Layer depths of H-TESSEL's hydrological scheme [cm]: 7, 21, 72, and 189

Table 2: Input variables for the CMEM to compute TBs at TOA.

Soil conditions	Constant fields	Soil texture fraction [%]
		Orography [km]
Vegetation	Constant fields	High and low vegetation types
		High and low vegetation fractions
		Water fraction
	Dynamic fields	Low vegetation LAI
Meteorology	Dynamic fields	Soil moisture profile [m^3m^{-3}]
		Soil temperature profile [K]
		Skin temperature [K]
		Snow depth [m]
		Snow density [kgm^{-3}]
		2 m temperature [K]

Table 3: TB filtering criteria to keep data, applied to the TB signals.

* The slope is at the model T225 spectral horizontal resolution (~80km).

TB_{OR}	TB_{HT}	All TB signals
ORCHIDEE's daily average surface temperature > 275 K	Snow water equivalent < 0.01 m	Daily TB < 300 K
ERA-Interim's daily average 2 m air temperature > 273 K	ERA-Interim's daily average 2 m air temperature > 273.5K	Mask (from SMOS's L2 product)
	Orography (slope)* < 0.04	

Table 4: Mean temporal and spatial correlations for SSM (Polcher et al., 2016) and the horizontal and vertical polarization of TBs over the Iberian Peninsula from 2010 to 2012.

	Temporal		Spatial	
	Horizontal	Vertical	Horizontal	Vertical
TB_{OR} vs. TB_{SM}	0.75	0.76	0.20	0.30
TB_{HT} vs. TB_{SM}	0.82	0.82	0.24	0.29
$TB_{HT(VC)}$ vs. TB_{SM}	-	-	0.17	0.36
$TB_{OR(SD)}$ vs. TB_{SM}	-	-	0.22	0.33
$TB_{OR(FW)}$ vs. TB_{SM}	-	-	0.20	0.30
SSM_{OR} vs. SSM_{SM}	0.81		0.28	

Table 5: Spatial correlation for the first and second variation modes of the EOF analyses performed for the difference between modelled and measured TBs. TBH and TBV correspond to the horizontal and vertical polarizations, respectively.

	Mode 1	Mode 2
$TB_{OR} - TB_{SM}$ (TBH) vs. $TB_{OR} - TB_{SM}$ (TBV)	0.99	0.97
$TB_{HT} - TB_{SM}$ (TBH) vs. $TB_{HT} - TB_{SM}$ (TBV)	0.86	0.75
$TB_{OR} - TB_{SM}$ (TBH) vs. $TB_{HT} - TB_{SM}$ (TBH)	0.92	0.69
$TB_{OR} - TB_{SM}$ (TBV) vs. $TB_{HT} - TB_{SM}$ (TBV)	0.73	0.48

Table 6: Possible explanations studied and proposed to analyze the dominant mode of the error between measured and modelled TBs. The paper's section where these are analyzed has been included.

* EOF analysis → Incompatible spatio-temporal variability of errors.

Hypotheses			Outcome (test)	Section
Biases in precipitation forcing			Discarded (EOF analysis*)	4.2.2
Errors in LST modelling			Discarded (EOF analysis* & annual cycle over southern and northern IP)	4.2.2 & 4.3
CMEM configuration	Vegetation cover		Discarded (EOF analysis* & spatial correlation)	4.2.3
	Soil discretization		Discarded (EOF analysis*)	
	ε parametrization	Combined effect of the Fresnel law and Wigneron et al. (2001) to estimate ε_s and T_{eff}.	Discarded (EOF analysis* & spatial correlation)	
		Є estimation	Proposed to study	5
		τ_{veg} estimation	Proposed to study	
		ε_r estimation	Proposed to study	
Modelled LAI			Discarded	
Rainfall interception			Discarded	
Attenuation effect of litter in measured TB			Discarded	
LSMs' subgrid processes simplifications			Discarded	
Instrumental issues (RFIs)			Discarded	

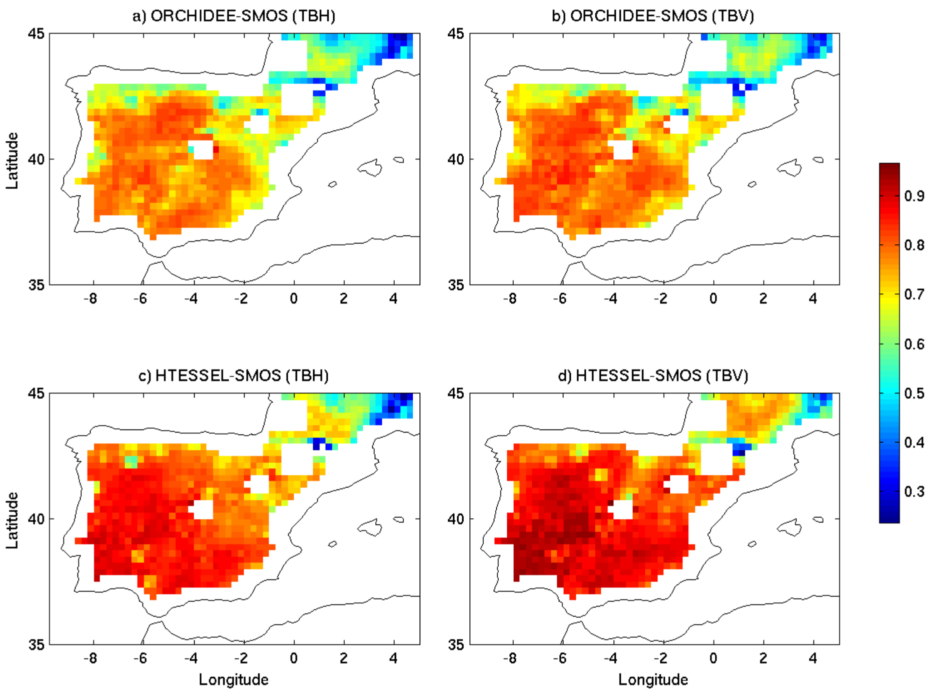

Figure 1: Temporal correlation between modelled and measured TBs from 2010 to 2012. TBH and TBV correspond to the horizontal and vertical polarizations, respectively.

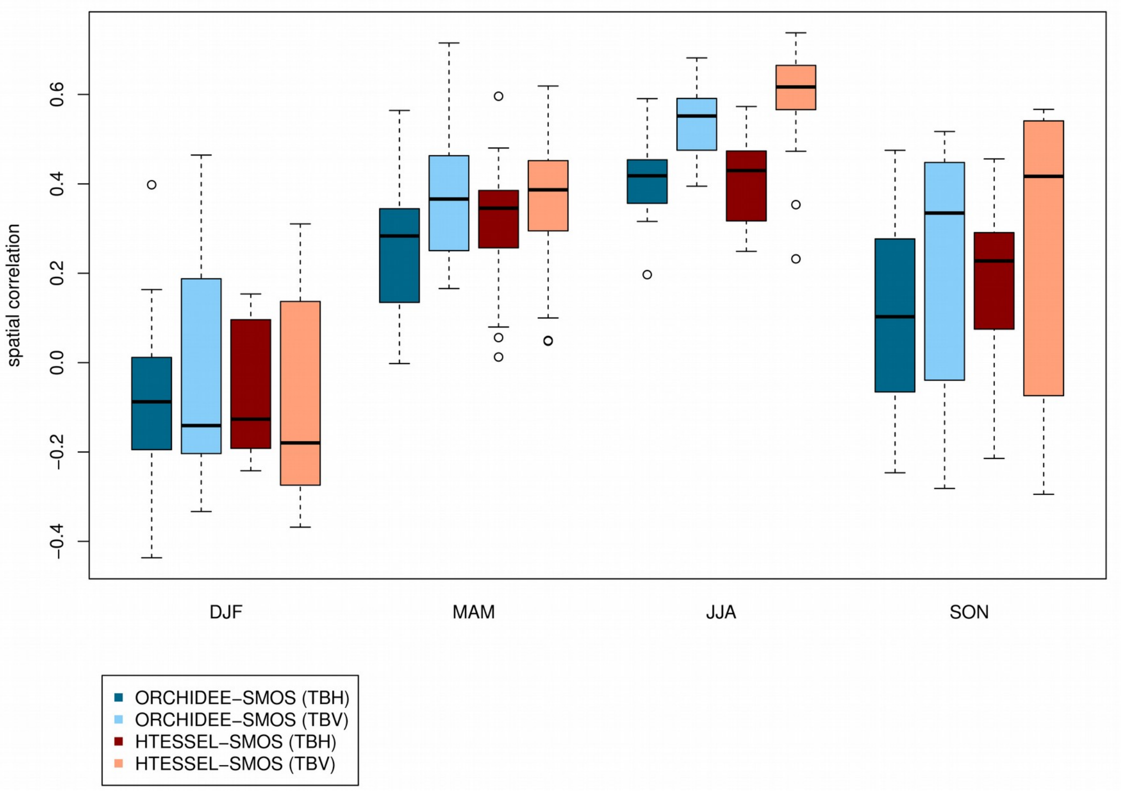

Figure 2: Boxplot showing the annual cycle of the spatial correlation between modelled and measured TBs, over the Iberian Peninsula from 2010 to 2012. TBH and TBV correspond to the horizontal and vertical polarizations, respectively. Values have been grouped per seasons: winter (DJF), spring (MAM), summer (JJA), and fall (SON).

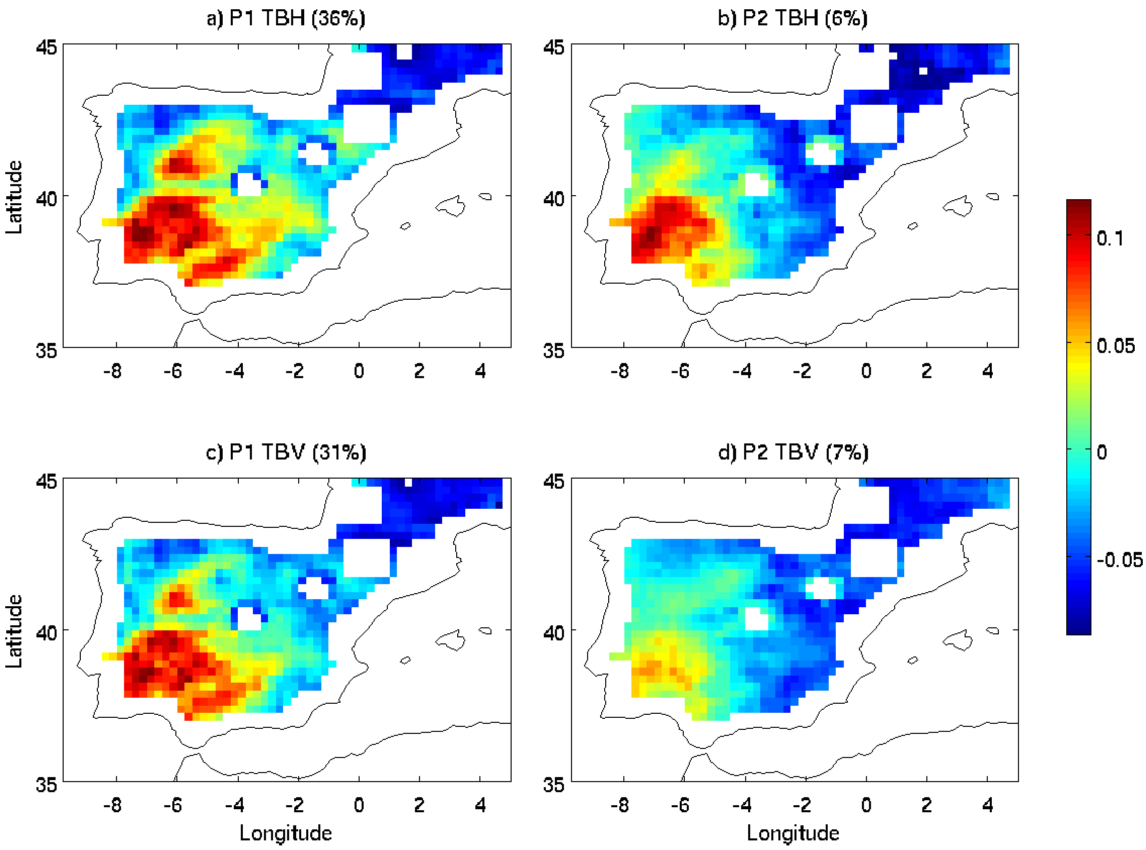

Figure 3: Spatial patterns associated with the first two EOF variation modes (P1 and P2) of the difference between modelled TB (ORCHIDEE) and measured TB (SMOS). TBH and TBV correspond to the horizontal and vertical polarizations, respectively. The percentage of variance explained by each mode is included in brackets.

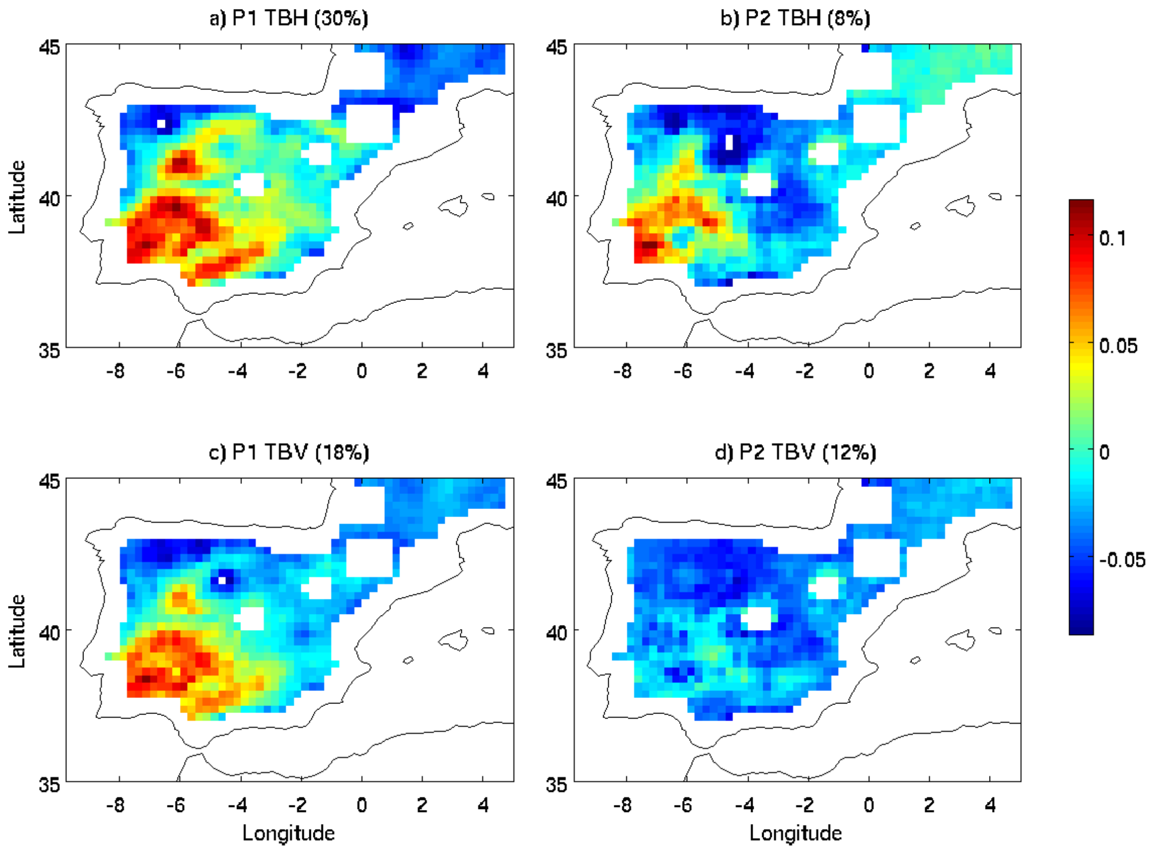

Figure 4: As Figure 3 but for H-TESSEL.

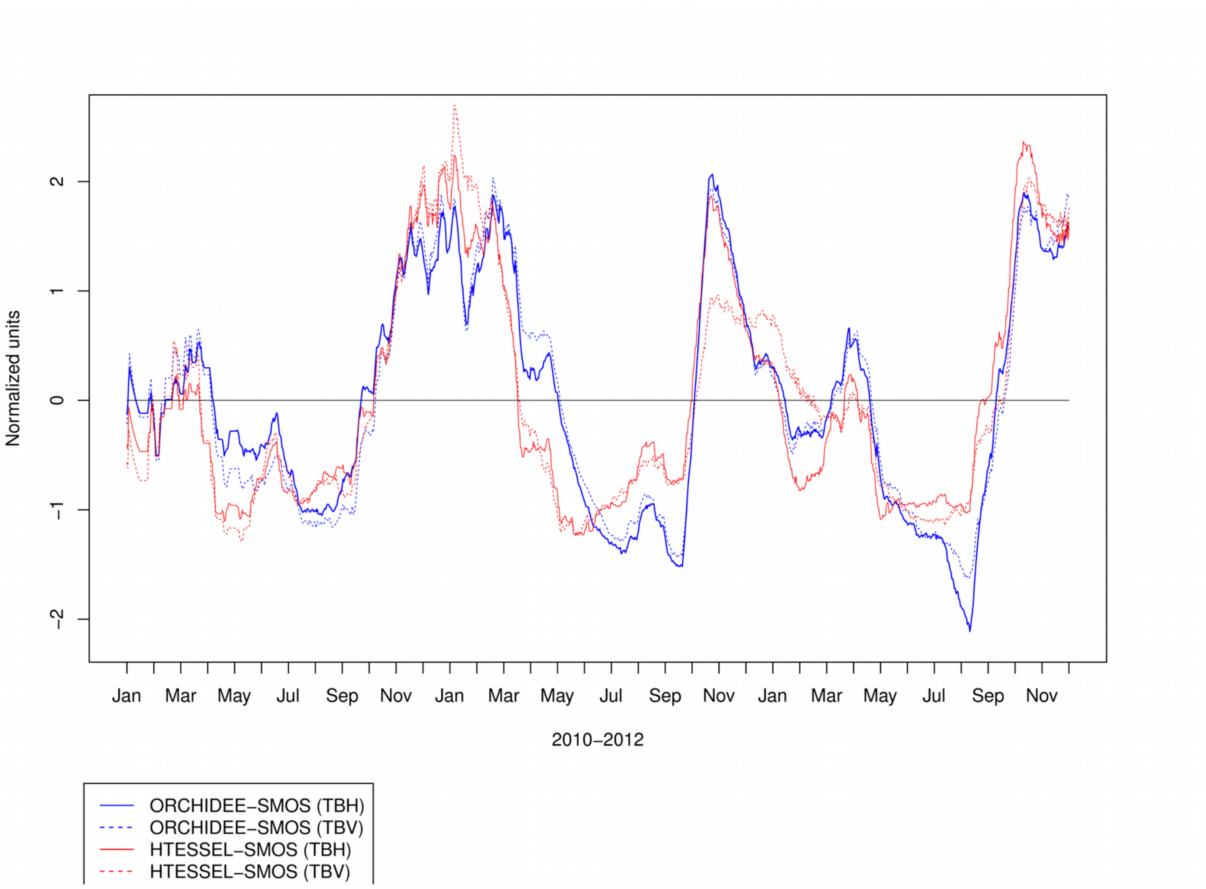

Figure 5: Temporal evolution of the expansion coefficients correspondent to the first EOF variation mode of the TB errors (ORCHIDEE versus SMOS and H-TESSEL versus SMOS) over the Iberian Peninsula. Values have been normalized using the standardization method. TBH and TBV correspond to the horizontal and vertical polarizations, respectively.

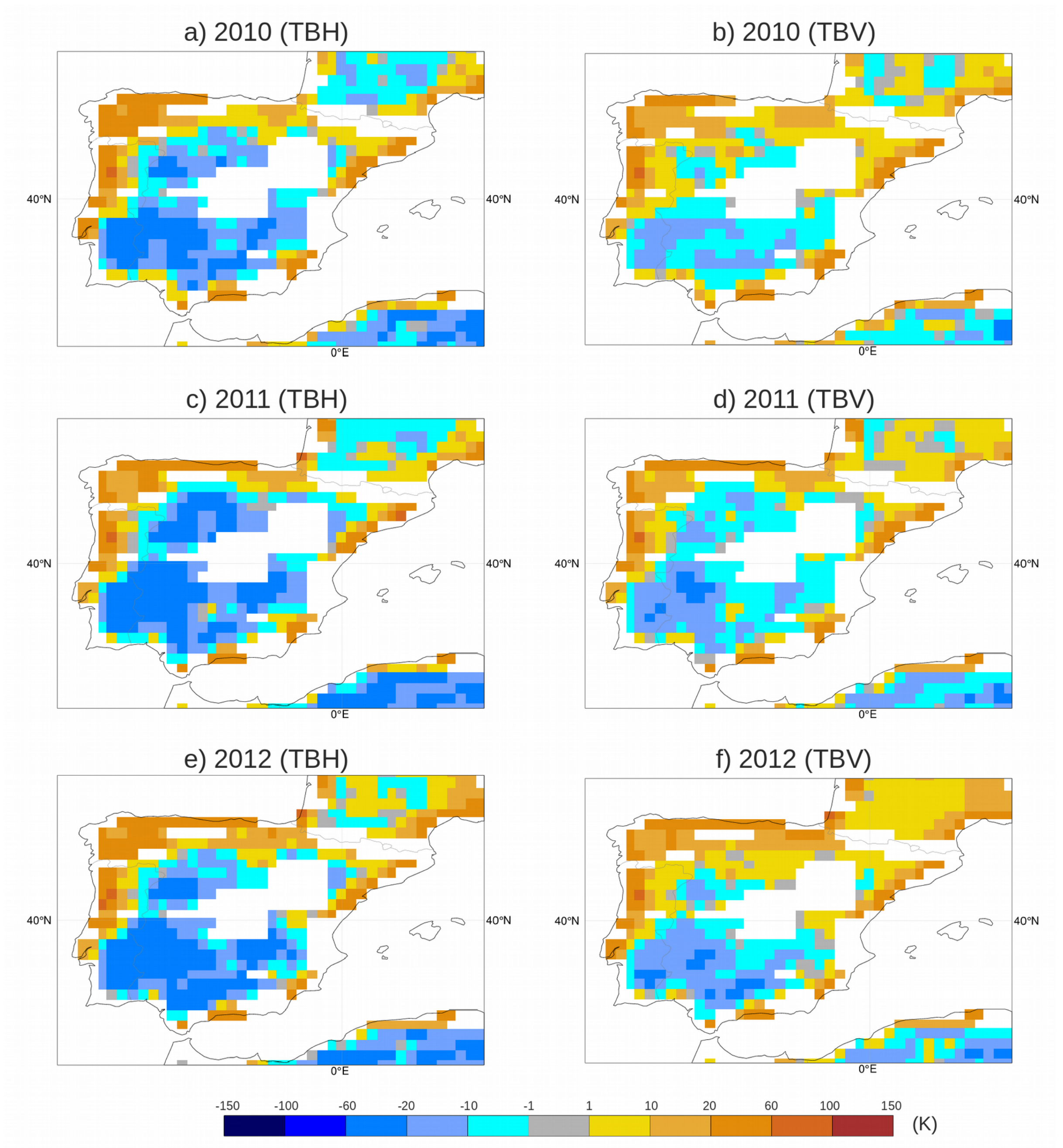

Figure 6: ECMWF's mean error (observation-model) from the months of November 2010 to 2012. TBH and TBV correspond to the horizontal and vertical polarizations, respectively.

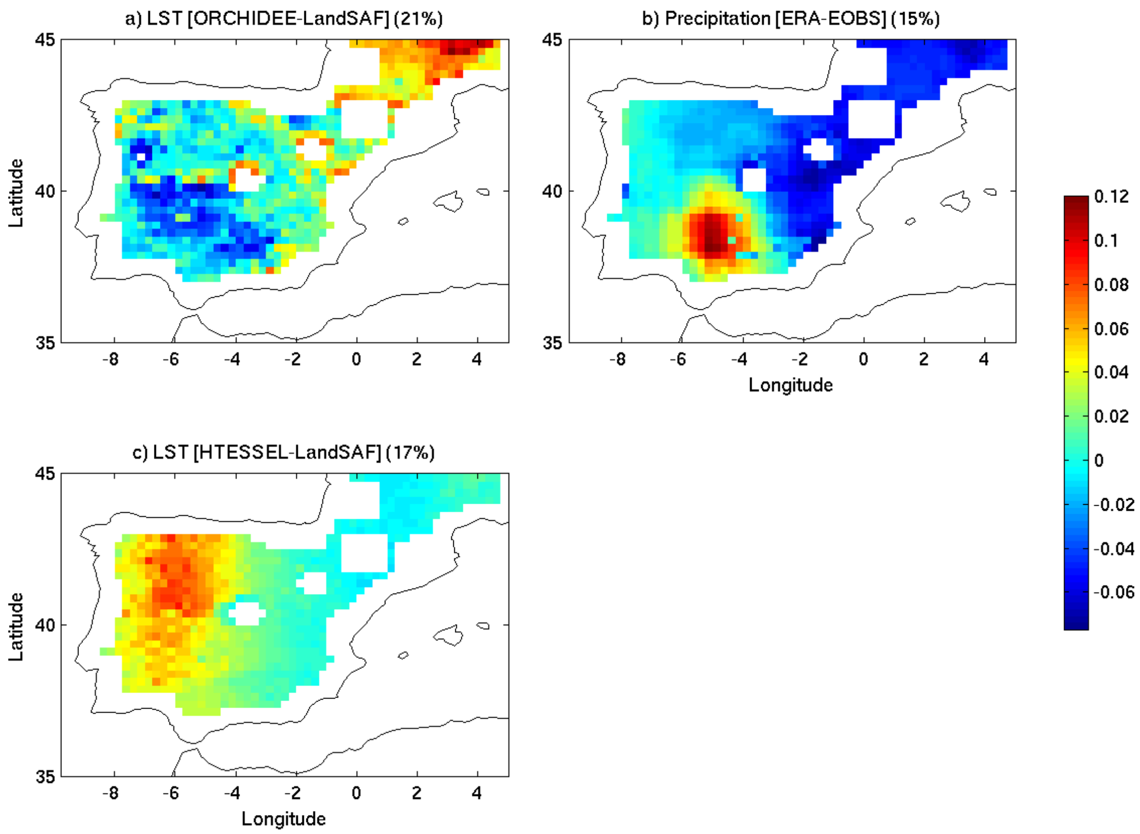

Figure 7: Spatial patterns from the first EOF variation mode of the LST and the precipitation errors. The percentage of variance explained by each mode is included in brackets.

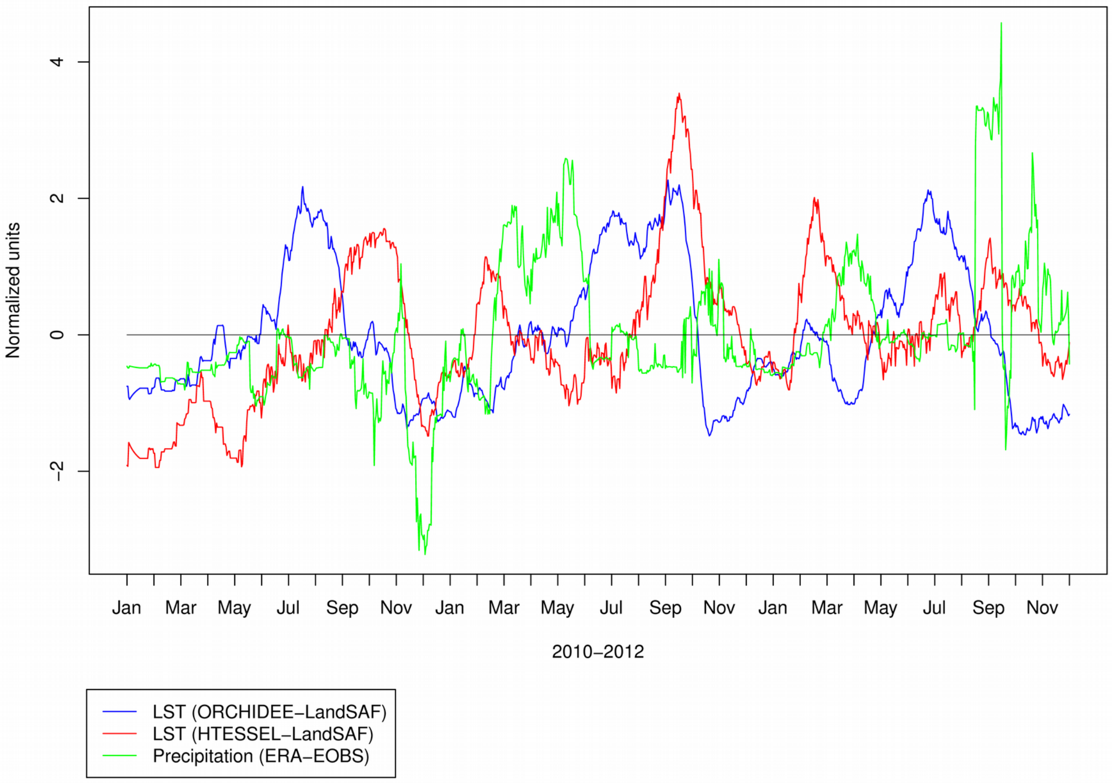

Figure 8: Temporal evolution of the expansion coefficients correspondent to the first EOF variation mode of the LST and the precipitation errors. As in Fig. 5, values have been normalized using the standardization method.

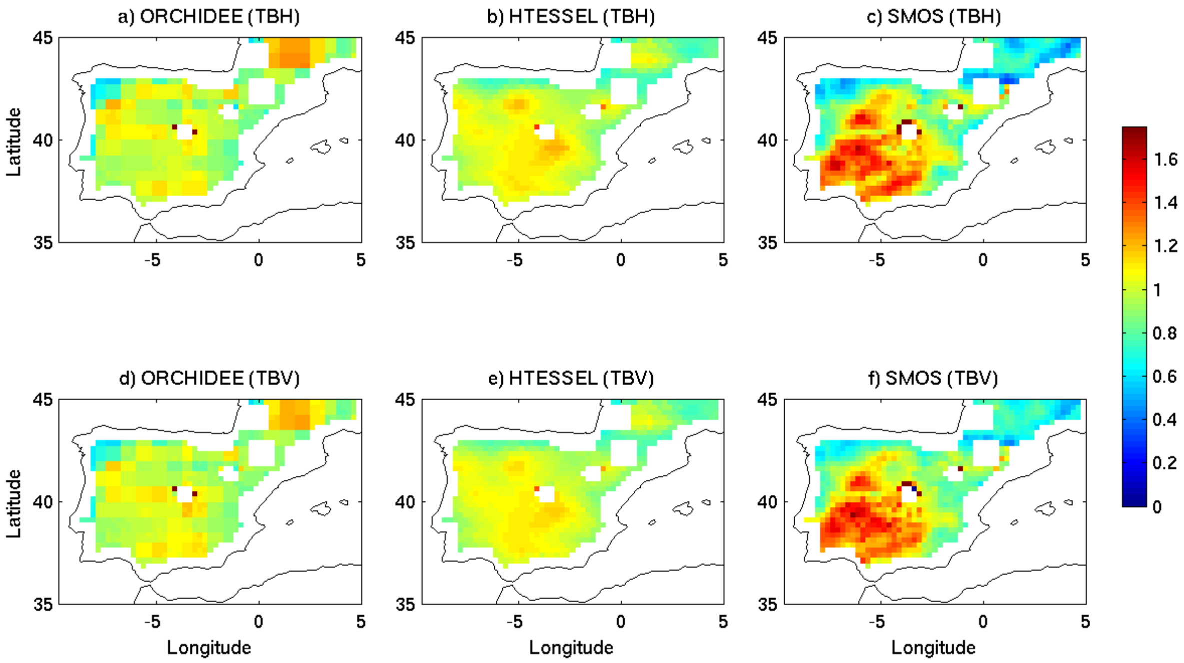

Figure 9: Normalized amplitude of the smoothed annual cycle of modelled and measured TBs: $amplitude(TB)/\overline{TB}$. TBH and TBV correspond to the horizontal and vertical polarizations, respectively.

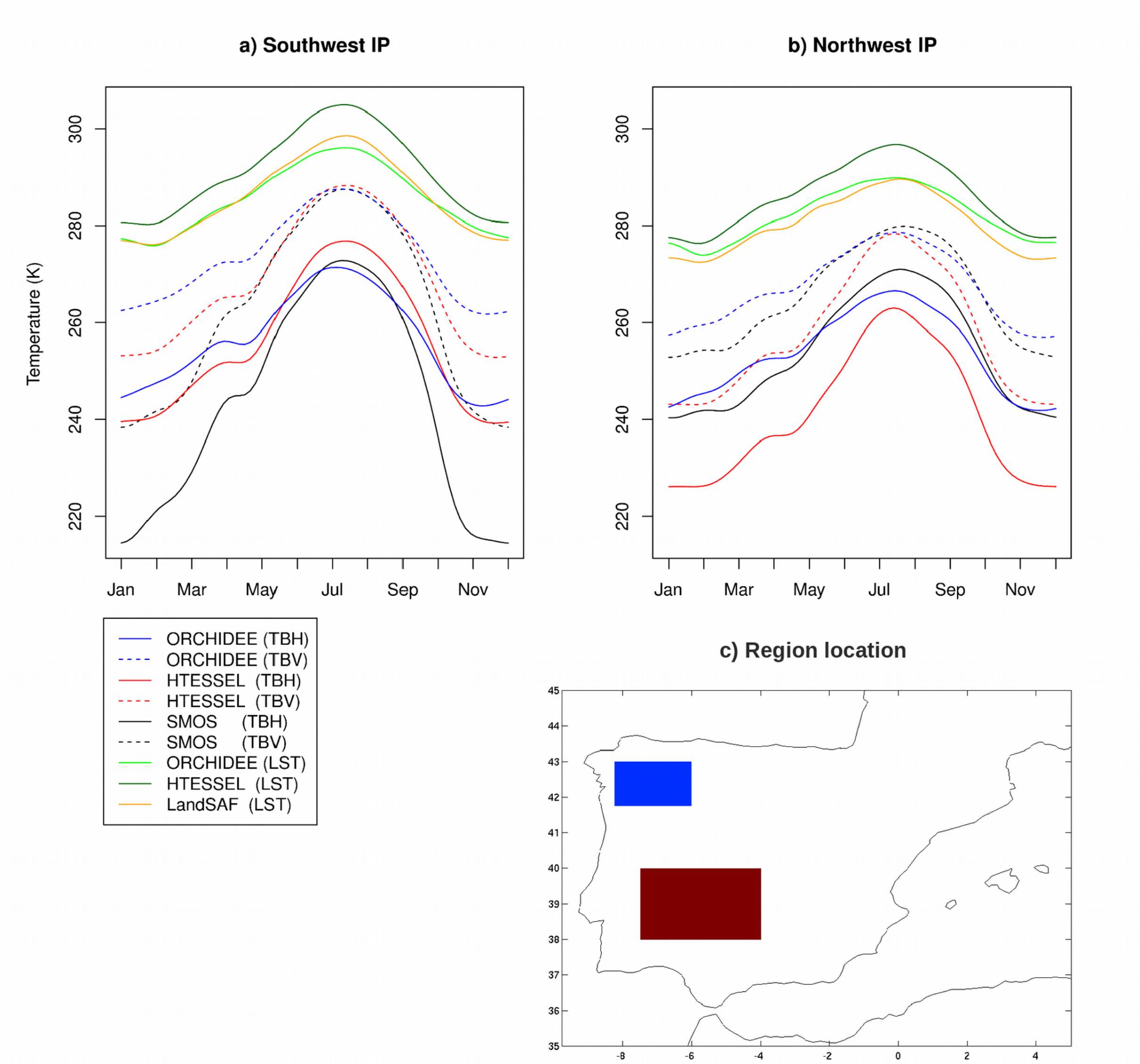

Figure 10: Smoothed annual cycle of TB_{SM}, TB_{OR}, and TB_{HT}, as well as of the LST signals from ORCHIDEE, H-TESSEL, and LandSAF over a southwestern (a) and northwestern (b) region of the Iberian Peninsula, from 2010 to 2012. The TBH and TBV correspond to the horizontal and vertical polarizations, respectively. The regions' location is shown in figure c: southwest (red) and northwest (blue).